



Efficient CO₂ photoreduction triggered by oxygen vacancies in ultrafine Bi₅O₇Br nanowires

Danjuan Mao^{a,1}, Shuxue Yang^{a,1}, Yuan Hu^a, Huan He^b, Shaogui Yang^b, Shourong Zheng^a, Cheng Sun^a, Zhifeng Jiang^{c,d,*}, Xiaolei Qu^{a,**}, Po Keung Wong^{c,e,*}

^a State Key Laboratory of Pollution Control and Resource Reuse, School of the Environment, Nanjing University, Nanjing 210023, China

^b School of Environment, Nanjing Normal University, Nanjing 210023, China

^c School of Life Sciences, The Chinese University of Hong Kong, Shatin, NT, 999077, Hong Kong Special Administrative Region of China

^d Institute for Energy Research, Jiangsu University, Zhenjiang 212013, China

^e Institute of Environmental Health and Pollution Control, School of Environmental Science & Engineering, Guangdong University of Technology, Guangzhou 510006, China

ARTICLE INFO

Keywords:

CO₂ reduction
Bi₅O₇Br nanowires
Charge separation
Oxygen vacancies
Photocatalysis

ABSTRACT

Sluggish charge kinetics, poor photoabsorption and low CO₂ affinity have been regarded as the main obstacles inhibiting the efficiency of CO₂ photoreduction. Herein, freestanding ultrafine Bi₅O₇Br nanowires with abundant oxygen vacancies were initially fabricated to synchronously optimize these critical processes. The 1D ultrafine configuration and abundant oxygen vacancies endow the Bi₅O₇Br nanowires with extended photoadsorption, boosted charge separation and enhanced interfacial CO₂ adsorption and activation. Density functional calculations reveal that the presence of oxygen vacancies on the Bi₅O₇Br surface can not only afford abundant localized electrons and lower the CO₂ reaction energy barriers, but also have a stronger covalent interaction and more efficient electron exchange and transfer between CO₂ and oxygen vacancies. Without any co-catalyst or sacrifice reagent, OV-rich Bi₅O₇Br nanowires show a 27.76-fold enhancement of CO₂ photoreduction activity relative to bulk Bi₅O₇Br in the gas-solid system. This work may inspire the future design of ultrafine catalysts for artificial photosynthesis.

1. Introduction

The continuous accumulation of atmospheric carbon dioxide (CO₂) destroys the natural carbon balance and exacerbates global warming, being a global challenge and pressing issue [1–4]. Inspired by the nature photosynthesis, photocatalytic reduction of inert CO₂ into value-added carbon chemicals, which relies on photogenerated electrons and/or holes to trigger the cleaving of chemical bonds under ambient conditions, has been considered as a sustainable and appealing approach to remit both the energy demands and environmental crisis [5–8]. Unfortunately, the CO₂ photoconversion is still subjected to poor efficiency for practical implementation due to the highly negative reduction potential of – 1.9 V versus reversible hydrogen electrode (NHE) for the formation of reactive •CO₂ and the sluggish dynamics of involved proton-assisted multi-electrons transfer processes [9–11]. Therefore, to achieve an

efficient photoreduction of CO₂, boosting the charge separation efficiency, extending the photo-absorption and building surface reactive sites for promoting CO₂ activation and conversion may be viable strategies.

Recently, one-dimensional (1D) atomic-scale nanomaterials with considerable advantages were emerging as a class of promising photocatalysts [12–14]. The atomic thickness with accompanied ultra-large specific surface area allows efficient light harvesting. The ultrafine configuration can substantially suppress the recombination of electron-hole pairs due to the shortened bulk carrier diffusion length. Moreover, ultrafine 1D nanostructure provides a direct path for electron transport along the axial direction, which is conducive to the separation of electron-hole pairs. In addition, for metal oxide semiconductors, when the thickness of materials decreases to quantum size, the exposed surface oxygen atoms in ultrafine nanostructures will be inclined to

* Corresponding authors at: School of Life Sciences, The Chinese University of Hong Kong, Shatin, NT, 999077, Hong Kong Special Administrative Region of China.

** Corresponding author.

E-mail addresses: ntjiangzf@sina.com (Z. Jiang), xiaoleiqu@nju.edu.cn (X. Qu), pkwong@cuhk.edu.hk (P.K. Wong).

¹ These authors contributed equally to this work.

escape to form defect structures, which could induce the formation of new defect levels and extend the photo-responsive range [9,15]. Moreover, the surface defects can induce the formation of abundant localized charges. These asymmetrically distributed surface charges form local polarized electric fields, which promote the rapid transfer of the trapped interfacial charge to the adsorbates. Furthermore, the defect sites also can serve as reactive centers to alter the charge density distribution, which could cause low-coordination edge sites and increase intermediate binding, and hence remarkably reduce the reaction energy barrier of CO₂ photoreduction [16,17]. In view of the aforementioned analysis, the quantum-sized materials with rich surface defects and abundantly exposed reactive sites could provide a prominent platform to synergistically address the adsorption and split issues during activation and conversion of CO₂. However, so far the generation of defects in photocatalysts is mainly acquired by subsequent heat treatment under inert atmosphere or vacuum, hydrogen atmospheric reduction, or ion doping, which often need rigorous conditions and complicated steps. Therefore, developing facile and convenient strategies for the one-step fabrication of favorable atomic vacancies is highly challenging and appealing.

Sillen-structured bismuth oxybromides have shown the promise in solar energy conversion and heterogeneous photocatalysis because the inherent internal electric field induced by dipoles in unit cells enables effective separation of electrons and holes [18,19]. Generally, increasing the content of bismuth in conventional BiOBr crystals enhances their optical absorption and reinforces the hybridization of the conduction band to promote electron transport [20]. Therein, Bi₅O₇Br possesses appropriate band gaps and conduction band level for driving CO₂ reduction, making it a promising candidate for solar-driven CO₂ reduction. However, to our knowledge, no previous work has investigated the photocatalytic properties of Bi₅O₇Br for CO₂ reduction, inspiring an exciting attempt and a detailed investigation. Besides, downsizing the Bi₅O₇Br into quantum size, the cations coordinated by high density oxygen atoms are potential clusters for the formation of oxygen vacancies (OVs) under mild conditions [21,22]. In this work, ultrafine topologies of Bi₅O₇Br nanowires with abundant oxygen vacancies have been initially prepared via a facile and straightforward hydrothermal process without using surfactants or organic solvents. The one-dimensional (1D) ultrafine scaffolds can substantially suppress bulk recombination of electron-hole pairs due to the shortened carrier diffusion distance. The introduction of OVs not only affords abundant localized electrons, but also reinforces covalent interaction and electron exchange and transfer with CO₂ molecules. Expectedly, OV-rich Bi₅O₇Br nanowires exhibited a remarkable 27.76 times improved photoreduction activity than the bulk counterparts. The deep insight of the enhanced CO₂ photoreduction over ultrafine nanowires was further unraveled by experimental and theoretical results.

2. Experimental section

2.1. Sample preparation

2.1.1. Synthesis of OV-rich ultrafine Bi₅O₇Br nanowires

In a typical experiment, 0.4 mmol 1-Octyl-3-methylimidazolium bromide (OmimBr) were added into 20 mL mannitol solution (0.1 M) at room temperature under vigorous stirring for 60 min. Subsequently, a homogeneous solution was obtained when the Bi(NO₃)₃·5 H₂O solution (2 mmol Bi(NO₃)₃·5 H₂O dissolved into 5 mL of 1 M HNO₃ solution) was added dropwise into the above reacted system with continuous stirring and the pH value of the solution was adjusted to 11 with 2 M NaOH. The mixture was stirred for 60 min at room temperature and then transferred into a 50 mL Teflon-lined autoclave, sealed and heated at 120 °C for 6 h. The product was collected, washed thoroughly with ethanol and deionized water for many times, and then dried at 60 °C in vacuum overnight for further characterization.

2.1.2. Synthesis of OV-poor ultrafine Bi₅O₇Br nanowires

In a typical experiment, 0.4 mmol OmimBr were added into 20 mL mannitol solution (0.1 M) at room temperature under vigorous stirring for 60 min. Subsequently, a homogeneous solution was obtained when the Bi(NO₃)₃·5 H₂O solution (2 mmol Bi(NO₃)₃·5 H₂O dissolved into 5 mL of 1 M HNO₃ solution) was added dropwise into the above reacted system with continuous stirring and the pH value of the solution was adjusted to 11 with 2 M NaOH. The mixture was stirred for 60 min at room temperature and then transferred into a 50 mL Teflon-lined autoclave, sealed and heated at 120 °C for 6 h. The product was collected, washed and then oxidized with hydrogen peroxide (H₂O₂) (2 mL, 10%) by ultrasound for 10 min and stirring for 3 h. Subsequently, the sample was washed thoroughly with ethanol and deionized water for many times, and then dried at 60 °C in vacuum overnight for further characterization.

2.1.3. Synthesis of bulk Bi₅O₇Br

Typically, 2 mmol Bi(NO₃)₃·5 H₂O and 1 mmol OmimBr were added into 25 mL deionized water and stirred for 30 min at room temperature. The pH value of the above solution was adjusted to 13 with 2 M NaOH under continuous stirring. Subsequently, the mixture was poured into 50 mL autoclave, sealed and heated at 160 °C for 12 h, and then cooled naturally. The resulting precipitate was collected, washed consecutively with absolute ethanol and deionized water several times, and then dried in vacuum at 60 °C overnight for further characterization.

2.2. Characterization

The transmission electron microscopy (TEM) images and the high-angle annular dark-field scanning transmission electron microscopy (HAADF-STEM) images were obtained on a (S)TEM Titan cubed instrument with a field emission source and probe forming aberration corrector (FEI TF20). The powder X-ray diffraction (XRD) patterns of the Bi₅O₇Br samples were recorded on a Bruker D8-advance X-ray diffractometer equipped with Cu-Kα radiation (λ = 1.5406 Å). The scanning electron microscope (SEM) images were carried out by QUANTA FEG 250. X-ray photoelectron spectroscopy (XPS) measurements were performed on a PHI5000 Versa Probe electron spectrometer with an excitation source of Al Kα (ULVAC-PHI, Japan). The binding energy was corrected by using the contaminant carbon (C1s = 284.6 eV) as a reference. The room-temperature UV-vis absorption spectra were recorded on a UV-3600 spectrophotometer (Shimadzu, Japan) with BaSO₄ as a reference. Electron paramagnetic resonance (EPR) spectra were conducted on a Bruker model ESR JES-FA200 spectrometer at room temperature. CO₂ adsorption measurements were carried out by TriStar II 3flex gas adsorption analyzer. Room temperature photoluminescence (PL) spectra were collected at an excitation wavelength of 365 nm on a HORIBAFLuoroMax-4. Time-resolved fluorescence decay spectra of products were recorded on a multifunction fluorescence spectrometer (FLS1000, Edinburgh Instruments). *In-situ* Fourier-transform infrared (FTIR) measurements were carried out on a TMO Nicolet iS10 apparatus with an in-situ Harrick IR cell, and the resolution used for in-situ FTIR is 0.5 cm⁻¹. Surface photovoltage (SPV) spectra were measured by a self-made instrument equipped with a 500 W xenon lamp as the light source (CHF XM500W, Beijing Perfectlight Technology Co., Ltd), a three-grating monochromator (SBP300, Beijing Zolix Instrument Co., Ltd) and a lock-in amplifier (SR830-DSP) with the light chopper (SR540) to amplify the photovoltage signal and photovoltaic cell.

2.3. Photoelectrochemical measurements

The transient photocurrent response and electrochemical impedance spectroscopy (EIS) were measured on an electrochemical workstation (CHI-760E, Chenhua Instruments Co., Ltd.). It was performed in standard three-electrode system with commercial Ag/AgCl electrode as the

reference electrode and platinum (Pt) wire as the counter electrode, respectively. Working electrodes were prepared by a drip-coating method as follows: 20 mg of the catalysts was completely dispersed in 3 mL ethanol by sonication for 5 h to form a homogeneous colloid. Subsequently, the obtained colloid was added on the pretreated ITO slice ($1.0 \times 1.0 \text{ cm}^2$) and dried at 60°C in air for 6 h. The electrolyte was 0.1 M Na_2SO_4 solution and a 300 W Xenon lamp was taken as simulated solar light. EIS data was recorded at the open-circuit potential with the frequency range from 10^6 to 100 Hz. The photocurrent measurements were conducted by using the amperometric i-t curve mode with a bias voltage of 0.6 V for 600 s.

2.4. Density functional theory (DFT) calculation

DFT calculations were performed in the Vienna ab initio simulation package (VASP). A spin-polarized GGA PBE functional, a projector augmented wave (PAW) method and all-electron plane-wave basis sets with an energy cutoff of 400 eV were adopted. $\text{Bi}_5\text{O}_7\text{Br}$ is simulated using a surface model of p (2×2) unit cell periodicity. The Brillouin-zone integrations were sampled with a ($3 \times 3 \times 1$) Monkhorst-Pack mesh. The conjugate gradient algorithm was used in the optimization. The convergence threshold was set 1×10^{-4} eV in total energy and 0.05 eV/Å in force on each atom. The adsorption energy (E_{ads}) for CO_2 molecules was determined as follows: $E_{\text{ads}} = E_{\text{tot}} - (E_{\text{sur}} + E_{\text{mol}})$, where E_{tot} , E_{sur} and E_{mol} is the total energies for the adsorption state, pure surface and isolated molecule.

2.5. Photocatalytic CO_2 reduction

The photocatalytic CO_2 reduction activity was conducted in a gas-solid reaction system (Fig. S1) with the Labsolar 6 A closed circulation system (Beijing Perfectlight Technology Co., Ltd., China). In the CO_2 photocatalytic process, 20 mg $\text{Bi}_5\text{O}_7\text{Br}$ samples were dispersed in 10 mL of distilled water and dried on the surface of the quartz glass. Then, the quartz glass was placed on a triangle glass rack in the reaction cell. Subsequently, the reaction system was subjected to an exhaustive vacuum treatment and then pumped with high-purity CO_2 to reach atmospheric pressure. 2 mL deionized water was injected into the surface of catalyst for further photocatalysis. A 300 W xenon lamp coupled with an AM 1.5 G filter (PLS-SXE300UV, Beijing Perfectlight Technology Co., Ltd., China) was the light source. The irradiation spectrum of the Xenon lamp was shown in Fig. S2. The reaction temperature was controlled at 293 K by a recirculating cooling water system during irradiation (DC-0506, Shanghai Sunny Hengping Scientific Instrument Co., Ltd., China). Next, the product gas was taken out and qualitatively analyzed by a GC9790II gas chromatograph (Zhejiang Fuli Analytical Instrument Co., Ltd., China) equipped with a TDX-01 thermal conductivity detector (TCD) and a GDX-502 flame ionization detector (FID) with high purity N_2 as the carrier gas.

3. Results and discussion

3.1. Synthesis and micromorphology of $\text{Bi}_5\text{O}_7\text{Br}$ ultrafine nanowires

The $\text{Bi}_5\text{O}_7\text{Br}$ ultrafine nanowires were initially fabricated via a facile and straightforward hydrothermal process without using surfactants or organic solvents. The time-dependent evolution of nanowires has been investigated and provided in the Fig. S3. Before hydrothermal treatment, only bismuth-based amorphous nanodot precursor was obtained. Interestingly, upon heating, these bismuth-based amorphous nanodot precursor could gradually grow along a specific direction to form $\text{Bi}_5\text{O}_7\text{Br}$ ultrafine nanowire. Subsequently, with prolonged hydrothermal time to 6 h, the resulting $\text{Bi}_5\text{O}_7\text{Br}$ nanocrystals were completely converted to ultrafine nanowires. Note that ionic liquids may act as a passivating reagent to inhibit the growth of bismuth-based cores and preferentially adsorb to certain crystalline face of the primary bismuth-

based nanodots. Due to the different reactivity of crystallographic surfaces, the primary nanodots could further grow along a specific direction to form the resulting one-dimensional nanowires (Fig. 1a) [23]. Transmission electron microscopy (TEM; Fig. 1b-d) revealed the freestanding and well-defined nanowire structures with an average diameter around 5 nm (OV-rich $\text{Bi}_5\text{O}_7\text{Br}$ nanowires). In addition, the interplanar distance of 0.32 nm matched well with the (312) planes of orthorhombic $\text{Bi}_5\text{O}_7\text{Br}$ (Fig. 1e). The TEM-energy-dispersive X-ray spectrometry (EDS) elemental mappings of OV-rich $\text{Bi}_5\text{O}_7\text{Br}$ NWs suggested the homogeneous distribution of Bi, O, and Br elements over the OV-rich $\text{Bi}_5\text{O}_7\text{Br}$ NWs (Fig. 1f). For comparison, $\text{Bi}_5\text{O}_7\text{Br}$ ultrafine nanowires with similar grain size but lower oxygen vacancy concentrations were also obtained with a H_2O_2 treatment coupled infrared irradiation method (Fig. S4) (OV-poor $\text{Bi}_5\text{O}_7\text{Br}$ nanowires).

3.2. Characterization and theoretical prediction of oxygen vacancies in $\text{Bi}_5\text{O}_7\text{Br}$ ultrafine nanowires

The X-ray diffraction (XRD) pattern was used to further confirm the formation of $\text{Bi}_5\text{O}_7\text{Br}$. As displayed in Fig. 2a, all the peaks of the OV-rich and OV-poor $\text{Bi}_5\text{O}_7\text{Br}$ ultrafine nanowires can be indexed to orthorhombic $\text{Bi}_5\text{O}_7\text{Br}$ (JCPDS No. 38-0493), indicating the successful preparation of $\text{Bi}_5\text{O}_7\text{Br}$ nanowires. The large half peak width and feeble peak intensity relative to bulk $\text{Bi}_5\text{O}_7\text{Br}$ (Fig. S5) suggested the poor crystallinity, which was consistent with the ultrafine size.

To demonstrate the presence of oxygen vacancies, electron paramagnetic resonance (EPR) spectroscopy as an effective technique was employed to probe defective structures. The OV-rich $\text{Bi}_5\text{O}_7\text{Br}$ nanowires and OV-poor $\text{Bi}_5\text{O}_7\text{Br}$ nanowires have typical ESR signals centered at $g = 2.001$ (Fig. 2b), which can be ascribed to the electrons trapped in OVs [24,25]. Contrastingly, no detectable ESR signal was observed for bulk $\text{Bi}_5\text{O}_7\text{Br}$. The distinctly increased EPR signal from OV-rich $\text{Bi}_5\text{O}_7\text{Br}$ nanowires to OV-poor $\text{Bi}_5\text{O}_7\text{Br}$ nanowires evidences the increase of OVs concentration. Furthermore, X-ray photoelectron spectroscopy (XPS; Fig. 2c) was employed to determine the surface composition and chemical states. The peaks at about 529.6 eV and 532.3 eV originate from lattice oxygen and surface hydroxyl groups, respectively. In addition, a new peak of 530.9 eV appears in both $\text{Bi}_5\text{O}_7\text{Br}$ nanowires, which is assigned to the elevated adsorption of oxygen species near the OVs [26–28]. The larger peak area at 530.9 eV indicates the OV-rich $\text{Bi}_5\text{O}_7\text{Br}$ nanowires (25.7%) have much more oxygen vacancies than OV-poor $\text{Bi}_5\text{O}_7\text{Br}$ nanowires (20.5%). Furthermore, an evident shift to lower binding energy region is observed for OV-rich and OV-poor $\text{Bi}_5\text{O}_7\text{Br}$ nanowires in the high-resolution Bi 4f core spectra compared with bulk $\text{Bi}_5\text{O}_7\text{Br}$ (Fig. 2d). The downshift of Bi 4f orbitals illustrates the number of coordinating oxygen atoms is reduced by OV formation and the charge accumulation on Bi atom to compensate the charge nonequilibrium [15]. Based on the aforementioned results, we can safely conclude that the ultrafine $\text{Bi}_5\text{O}_7\text{Br}$ nanowires with rich oxygen vacancies have been successfully prepared. It provides an ideal 1D ultrafine configuration with rich surface defects and abundantly exposed reactive sites to facilitate the CO_2 photoreduction process.

To shed light on the effects of oxygen vacancies in $\text{Bi}_5\text{O}_7\text{Br}$ samples, UV/Vis diffuse reflectance spectra (DRS) were employed. As shown in Fig. 3a, the absorption edge of the OV-rich $\text{Bi}_5\text{O}_7\text{Br}$ nanowires significantly red-shifted relative to OV-poor $\text{Bi}_5\text{O}_7\text{Br}$ nanowires and bulk $\text{Bi}_5\text{O}_7\text{Br}$, which can be attributed to the existence of oxygen vacancies narrowing its band gap and the appearance of new defect levels in $\text{Bi}_5\text{O}_7\text{Br}$ ultrafine nanowires, similar phenomenon has been reported in previous literatures [9,29,30]. Accordingly, the Tauc plot suggests that the band gap of OV-rich $\text{Bi}_5\text{O}_7\text{Br}$ nanowires is 2.65 eV, which is obviously less than that of OV-poor $\text{Bi}_5\text{O}_7\text{Br}$ nanowires (2.74 eV) and bulk $\text{Bi}_5\text{O}_7\text{Br}$ (2.98 eV) (Fig. 3b). The relative energy-level position of VB maximum determined from XPS VB spectra is 1.56 eV for OV-rich $\text{Bi}_5\text{O}_7\text{Br}$ nanowires, 1.73 eV for OV-poor $\text{Bi}_5\text{O}_7\text{Br}$ nanowires and 2.02 eV for bulk $\text{Bi}_5\text{O}_7\text{Br}$ (Fig. S7a). Based on the above analysis, the CB

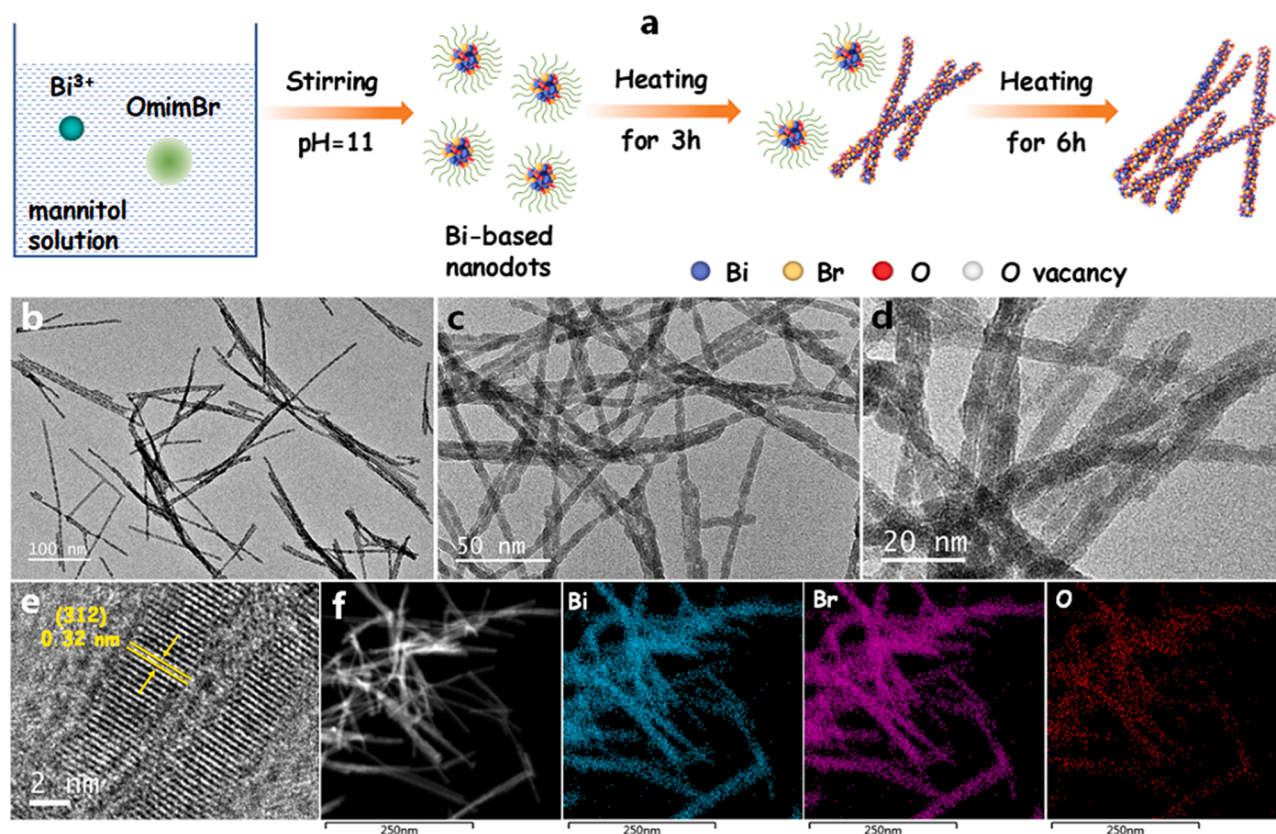


Fig. 1. (a) Illustration of the formation of OV-rich ultrafine $\text{Bi}_5\text{O}_7\text{Br}$ nanowires. (b-d) Representative TEM images, (e) HRTEM image of OV-rich $\text{Bi}_5\text{O}_7\text{Br}$ nanowires. (f) HADDF-STEM-EDS mapping of Bi, O, Br elements over OV-rich $\text{Bi}_5\text{O}_7\text{Br}$ nanowires.

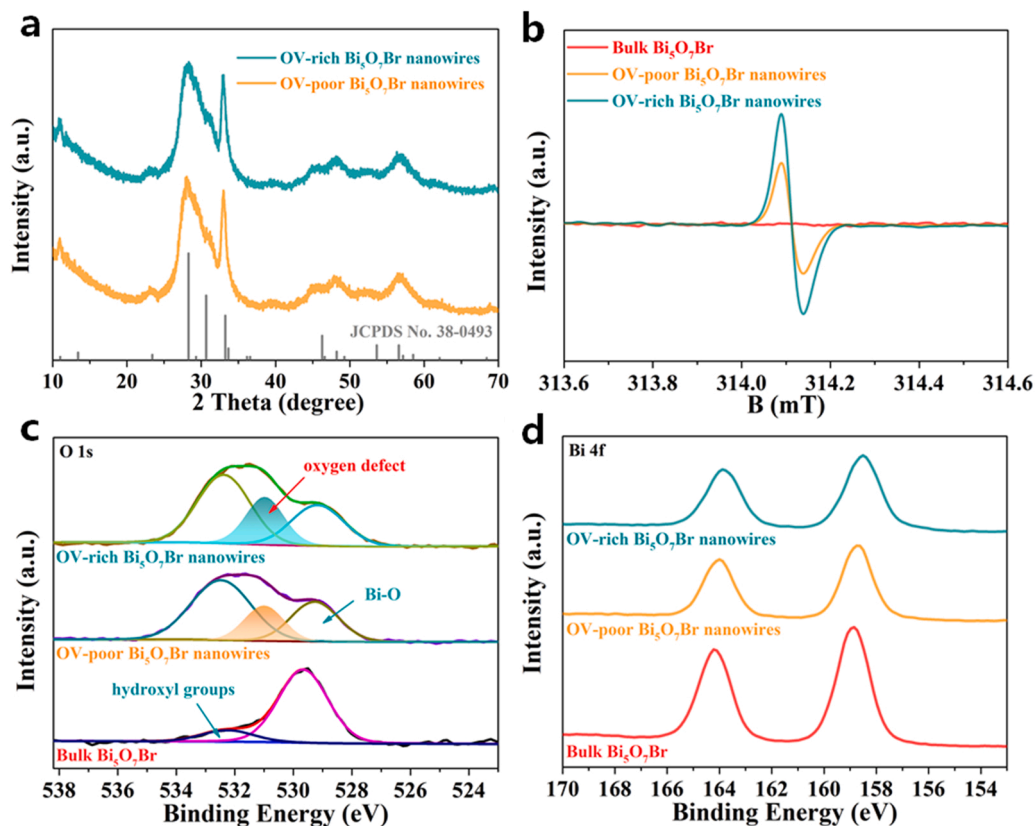


Fig. 2. Characterizations for OV-rich, OV-poor $\text{Bi}_5\text{O}_7\text{Br}$ nanowires and bulk $\text{Bi}_5\text{O}_7\text{Br}$. (a) XRD pattern, (b) EPR, (c) O 1s XPS and (d) Bi 4f XPS spectra.

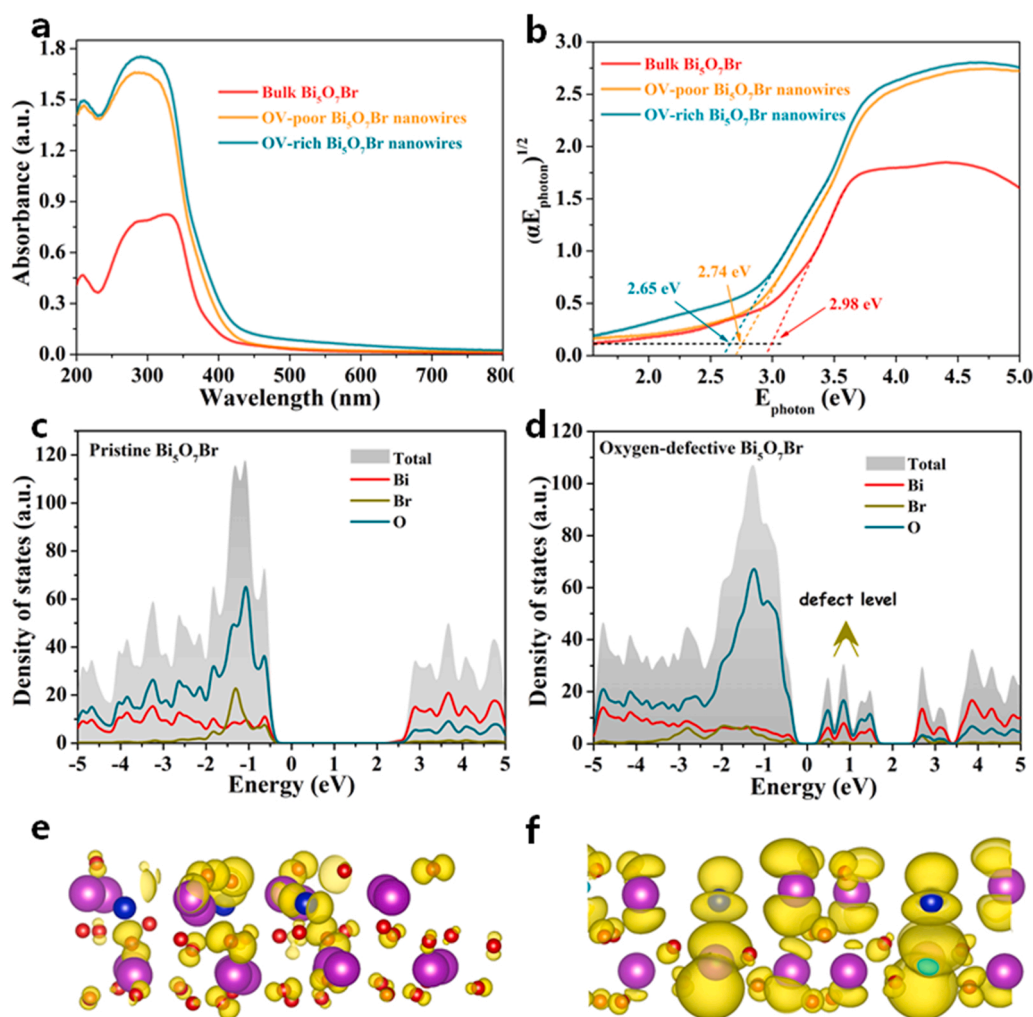


Fig. 3. (a) UV/Vis diffuse reflectance spectra and (b) tauc plots of the Bi₅O₇Br samples. (c-d) Calculated densities of states (DOS) and (e-f) the charge density contour plots of pristine and oxygen-defective Bi₅O₇Br.

potentials of OV-rich Bi₅O₇Br nanowires, OV-poor Bi₅O₇Br nanowires and bulk counterpart are calculated to be -0.96 , -1.01 and -1.09 eV, respectively (Fig. S7b). The improved light absorption and up-shift of CB are beneficial to trigger the photoreduction process.

To further uncover the possible electron structures changes of Bi₅O₇Br samples with oxygen vacancies, the projected density of states (PDOS) of pristine Bi₅O₇Br and oxygen-defective Bi₅O₇Br were thereby calculated. As displayed in Fig. 3c and d, the presence of oxygen vacancies brings about new defect levels near the valence band (VB), which endows Bi₅O₇Br narrowed band gap, hence favoring the photo-excited electrons to the conduction band (CB) and effectively promoting CO₂ photoreduction [31,32]. Moreover, as showed by the spatial distribution of charge density, the electrons neighboring oxygen vacancies become more delocalized relative to that of pristine Bi₅O₇Br, indicating that a local electric field is established by introducing oxygen vacancies and more effective carrier separation occurs [33]. The partial higher electron density in the vicinity of oxygen defects is beneficial to stabilize the reduction intermediates, and hence reduce the reaction energy barriers of CO₂ photoreduction (Fig. 3e,f) [34,35]. Based on the above advantages, it is highly desirable to fabricate ultrafine Bi₅O₇Br with abundant oxygen vacancies.

3.3. CO₂ photoreduction performance

In light of the above advantages, the solar CO₂ photoreduction

properties of the Bi₅O₇Br samples were evaluated in a gas-solid reaction system without photosensitizer or sacrifice reagent (Fig. 4a). Due to the facile occurrence of the two-electron CO reduction processes in comparison with eight-electrons CH₄ production pathway and unfavorable H₂O splitting in gas-solid reaction system, [33,36,37] all the Bi₅O₇Br samples produce CO as the dominant photoreduction product accompanied by a trace amount of CH₄ and H₂ (Fig. S8). Bulk Bi₅O₇Br has weak CO₂ photoreduction activity with a CO evolution rate of $0.58 \mu\text{mol g}^{-1} \text{h}^{-1}$. Contrastively, the CO yield of OV-rich Bi₅O₇Br nanowires steadily increases over time with a total CO yield of $108.24 \mu\text{mol g}^{-1}$ after a 6 h run. The average CO evolution rate of OV-rich Bi₅O₇Br NWs is up to $18.04 \mu\text{mol g}^{-1} \text{h}^{-1}$, which was 1.52 and 27.76 times higher than that of the OV-poor Bi₅O₇Br nanowires and bulk Bi₅O₇Br. The result highlights the superior performance of the ultrafine configuration and rich oxygen vacancies in improving the photofixation of CO₂. The CO evolution rate of OV-rich Bi₅O₇Br nanowires outperforms most previous results (Table S1). Moreover, the OV-rich Bi₅O₇Br nanowires ($68.65 \text{ m}^2 \text{ g}^{-1}$) possess similar BET surface areas as that of OV-poor Bi₅O₇Br nanowires ($64.53 \text{ m}^2 \text{ g}^{-1}$), which are much higher than that of bulk Bi₅O₇Br ($6.13 \text{ m}^2 \text{ g}^{-1}$) (Fig. S9). To distinguish the effect of surface area, we further calculated their specific activity (i.e., the mass activity normalized to the surface area). As shown in Fig. S10, the specific activity of OV-poor Bi₅O₇Br nanowires is still higher than bulk Bi₅O₇Br, demonstrating the collaborative contribution of 1D ultrafine structure induced axial charge transfer and oxygen vacancies on the separation of

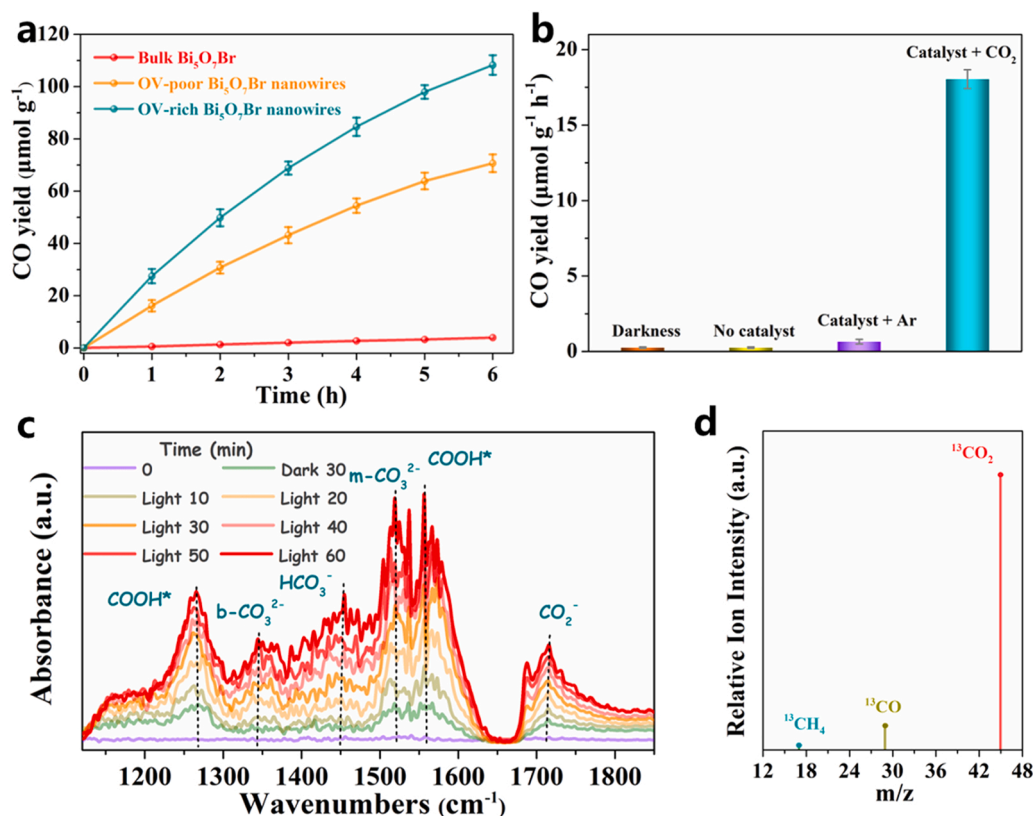


Fig. 4. (a) CO evolution along with irradiation times over Bi₅O₇Br samples. (b) The CO₂ photoreduction rates over OV-rich Bi₅O₇Br NWs under different conditions. (c) In situ FTIR spectra for the CO₂ reduction process on the OV-rich Bi₅O₇Br NWs. (d) Mass spectra of the products from the ¹³C₂O₂ isotope experiments.

photoinduced carriers. The further enhancement of specific activity for OV-rich Bi₅O₇Br nanowires relative to OV-poor Bi₅O₇Br nanowires could be contributed to the much larger amount of oxygen vacancies.

In addition, a set of control experiments is conducted to track the carbon source in the CO₂ reduction reaction (Fig. 4b). No detectable CO is generated in CO₂ photoreduction process without catalysts or in the dark, and a negligible amount of CO is produced under Ar condition ascribing to the organics attached on the photocatalysts. Additionally, an isotopic experiment was carried out using ¹³C-labeled CO₂ to probe the source of formed CO. As shown in Fig. 4d, the strong signal at *m/z* = 29 can be assigned to ¹³CO, which clearly confirms that the CO was generated from the photoreduction of ¹³CO₂. Besides, Bi₅O₇Br nanowires exhibit favorable durability with negligible activity decay and microstructure variation after 3 reaction cycles (Fig. S11–S13).

To gain deep insights into CO₂ photoconversion process, in situ Fourier transform infrared spectroscopy (FTIR) experiments are carried out to investigate the reaction intermediates over OV-rich Bi₅O₇Br nanowires. The strong peaks located at 2200–2400 cm⁻¹ can be ascribed to the asymmetric stretches of CO₂, indicating its favorable adsorption capability for CO₂ (Fig. S14) [37,38]. As shown in Fig. 4c, CO₂⁻ (1715 cm⁻¹), monodentate carbonate (m-CO₃²⁻; 1519 cm⁻¹), bidentate carbonate (b-CO₃²⁻; 1351 cm⁻¹) and bicarbonate (HCO₃⁻; 1456 cm⁻¹) formed and gradually increased with reaction time on OV-rich Bi₅O₇Br nanowires during the CO₂ photoreduction process, [39,40] demonstrating that CO₂ is continuously adsorbed and converted into carbon active species. In the meantime, the gradually strengthened peaks at 1262 and 1556 cm⁻¹ could be attributed to the vibrations of COOH* groups, which is the key intermediates during the photoreduction of CO₂ to CO [41,42]. Furthermore, the CO* absorption band at 2129 cm⁻¹ gradually increased with the extended irradiation time, collectively demonstrating the formation of CO product (Fig. S15) [43,44]. Lastly, as revealed in Fig. S16, the lower CO desorption temperature and significantly enhanced intensity in OV-rich Bi₅O₇Br nanowires

indicate that the formed CO* intermediates are more easily desorbed from the surface of Bi₅O₇Br nanowire, further explaining the enhanced CO₂ photoreduction activity.

3.4. Mechanism discussion

In order to provide further evidence to clarify the significantly improved CO₂ reduction performance, a string of photoelectrochemical characterizations are performed to investigate the charge separation and transfer behaviors. Surface photovoltage (SPV) spectroscopy is an effective and convincing mean to reveal charge separation efficiency of photoinduced carriers, in which magnitude of the SPV signal reflects the charge separation degree [45]. As depicted in Fig. 5a, OV-poor Bi₅O₇Br nanowires show an evidently magnified SPV signal than that of bulk Bi₅O₇Br, which is ascribed to the collaborative contribution of 1D ultrafine structure and surface oxygen vacancies on the separation efficiency of photoinduced carriers. The further improvement of SPV signal for OV-rich Bi₅O₇Br nanowires relative to OV-poor Bi₅O₇Br nanowires reveals that the surface oxygen vacancies can actually account for the greatly enhanced interfacial charge migration and separation efficiency. The charge carrier dynamics of the Bi₅O₇Br samples are further studied by time-resolved fluorescence emission decay spectra (Fig. 5b). The average lifetime is 1.39 ns for bulk Bi₅O₇Br, 5.82 ns for OV-poor Bi₅O₇Br nanowires and 7.23 ns for OV-rich Bi₅O₇Br nanowires, respectively, which indicates that OV-rich Bi₅O₇Br nanowires have highest charge separation efficiencies [46]. Moreover, as shown in Fig. 5c, the OV-rich Bi₅O₇Br nanowires exhibited the highest current density among the Bi₅O₇Br samples, with an instantaneous photocurrent response of about 1.81 μA cm⁻², in comparison to 1.25 and 0.19 μA cm⁻² for the OV-poor Bi₅O₇Br nanowires and bulk Bi₅O₇Br, respectively [47,48]. Furthermore, the smaller radius in the Nyquist circle and greatly decreased photoluminescence (PL) intensity also suggest a lower charge-transfer resistance and higher charge separation efficiency (Fig. 5d and e)

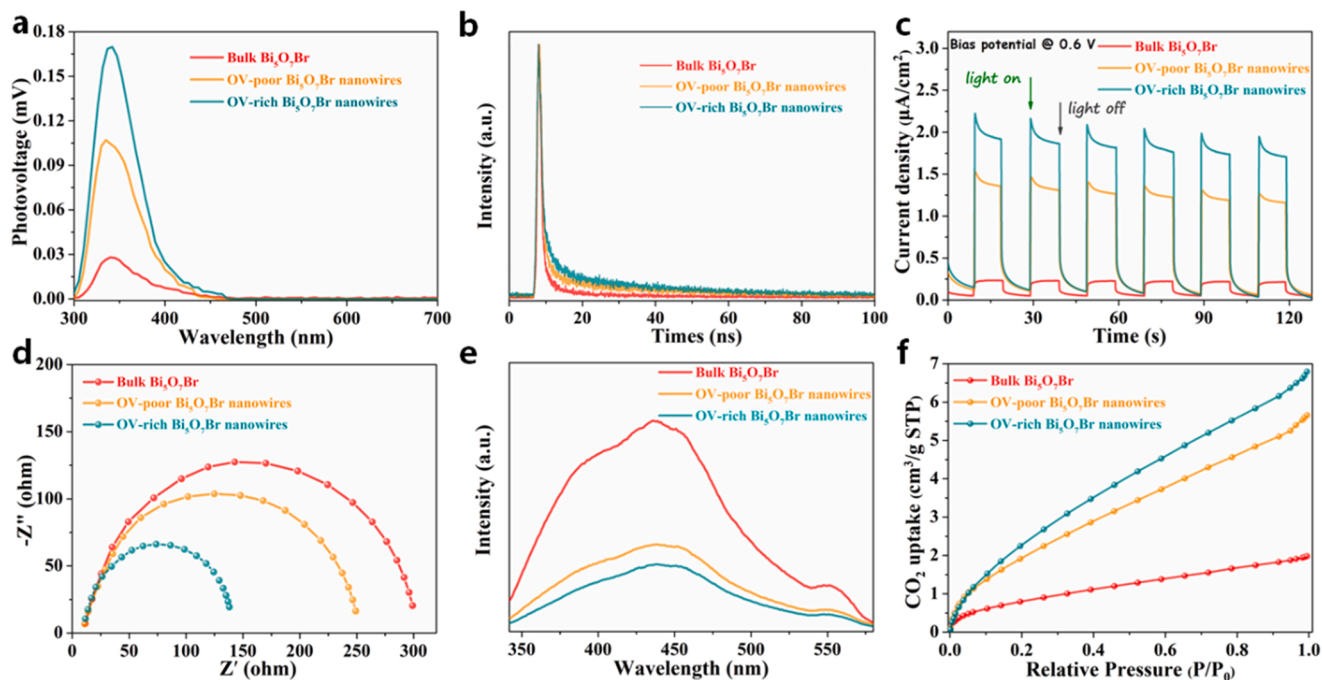


Fig. 5. (a) Surface photovoltage spectroscopy, (b) Fluorescence emission decay spectra, (c) Transient photocurrent responses, (d) Electrochemical impedance spectra, (e) Steady-state PL spectra and (f) CO₂ adsorption isotherms of the Bi₅O₇Br samples.

[49–51]. Overall, the multiple spectral results demonstrate that the abundant oxygen vacancies confined in ultrafine Bi₅O₇Br nanowires could actually improve the carrier separation and transport, thus rendering high CO₂ photoreduction efficiency.

To obtain an in-depth understanding of the interfacial CO₂ catalysis, CO₂ surface adsorption and activation processes are explored. Firstly, the CO₂ adsorption is generally regarded as the prerequisite for CO₂ photoreduction process. The presence of the higher oxygen vacancy concentration endowed OV-rich Bi₅O₇Br nanowires to be more negatively charged relative to OV-poor Bi₅O₇Br nanowires and bulk Bi₅O₇Br, leading to the better adsorption and activation of CO₂ on the surfaces. This can be further confirmed by the enhanced CO₂ adsorption capacity

of OV-rich Bi₅O₇Br nanowires in comparison with OV-poor Bi₅O₇Br nanowires and bulk Bi₅O₇Br (Fig. 5f). Moreover, in order to obtain information on catalytic sites at an atomic level, the CO₂ adsorption energies over the surface of pristine Bi₅O₇Br and oxygen-defective Bi₅O₇Br were calculated. As shown in Table S2, the adsorption energy on oxygen-defective Bi₅O₇Br is −0.392 eV, significantly lower than that on pristine Bi₅O₇Br (−0.198 eV). After CO₂ is adsorbed at the OV sites, the O-C-O angle is changed from 179.0° to 124.1°, and the C-O bond length is stretched from 1.166 Å to 1.293 Å. This means the C-O bonds are weakened in oxygen-defective Bi₅O₇Br. Furthermore, the charge difference distribution (Fig. 6a,b) exhibits that oxygen-defective Bi₅O₇Br has a stronger covalent interaction with CO₂, indicating a more efficient

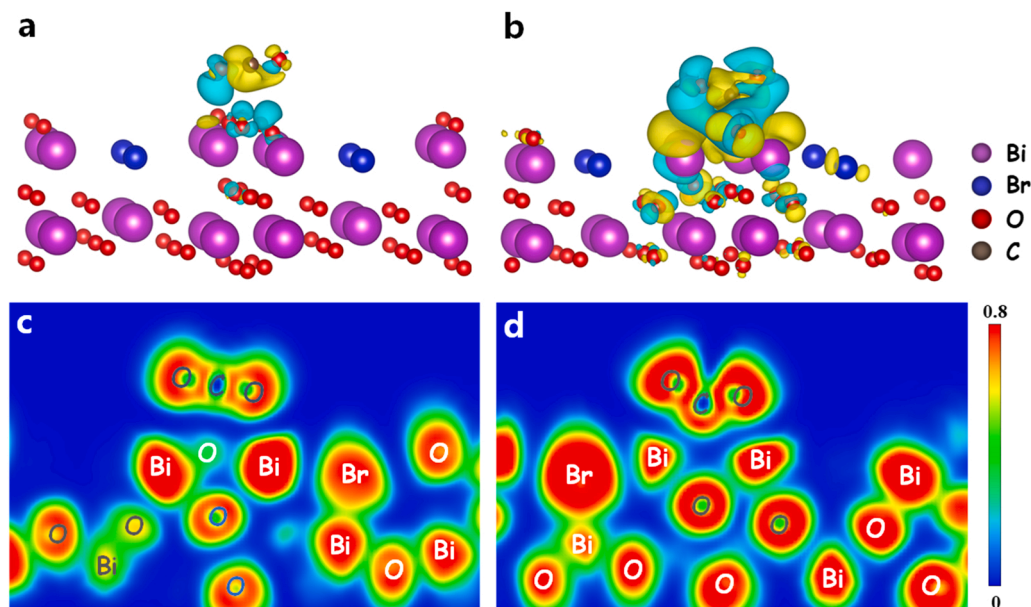


Fig. 6. Charge difference density of the adsorption of CO₂ molecules on (a) pristine Bi₅O₇Br and (b) oxygen-defective Bi₅O₇Br (charge accumulation is in blue and depletion in yellow, isosurface set at 0.005e Å^{−3}). Electron localization function (ELF) of (c) pristine Bi₅O₇Br and (d) oxygen-defective Bi₅O₇Br.

electron exchange and transfer process between CO₂ and OV. The electron localization function (ELF) also elucidates the presence of more covalent interaction between OVs of Bi₅O₇Br slab and CO₂. (Fig. 6c,d). Moreover, the total charge (Δq) of CO₂ is increased from $-0.013 e$ (pristine Bi₅O₇Br) to $-0.045 e$ (oxygen-defective Bi₅O₇Br), which implies that the CO₂ molecules in oxygen-defective Bi₅O₇Br obtain more electrons than in pristine Bi₅O₇Br, becoming activated and transferring to intermediates, thus promoting the CO₂ reduction reaction.

4. Conclusions

In summary, ultrafine topologies of Bi₅O₇Br nanowires with rich oxygen vacancies have been initially prepared via a facile and straightforward hydrothermal process without using surfactants or organic solvents. The 1D ultrafine scaffolds and abundant surface defects enable the Bi₅O₇Br nanowires with extended photoadsorption, increased charge separation efficiency, and promoted CO₂ adsorption and activation. DFT calculations revealed that oxygen-defective Bi₅O₇Br can not only afford abundant localized electrons and lower the CO₂ adsorption energies through stabilizing the intermediates on the Bi₅O₇Br surface, but also had a stronger covalent interaction and more efficient electron exchange and transfer between CO₂ and oxygen vacancies. As a result, OV-rich Bi₅O₇Br nanowires showed a favorable CO evolution rate of $18.04 \mu\text{mol g}^{-1} \text{h}^{-1}$, which was roughly 1.52 and 27.76 times higher than that of the OV-poor Bi₅O₇Br nanowires and bulk Bi₅O₇Br and also outperformed most previously reported outstanding photocatalysts. This work may inspire the future design of ultrafine catalysts for artificial photosynthesis.

CRediT authorship contribution statement

DanJun Mao: Conceptualization, Data curation, Funding acquisition, Investigation, Methodology, Visualization, Writing - original draft. **Shuxue Yang:** Data curation, Formal analysis, Investigation, Methodology, Validation. **Yuan Hu:** Data curation, Investigation, Methodology, Project administration, Software. **Huan He:** Formal analysis, Methodology, Resources. **Shaogui Yang:** Formal analysis, Methodology, Resources. **Shourong Zheng:** Formal analysis, Funding acquisition, Methodology, Resources. **Cheng Sun:** Conceptualization, Supervision, Writing - review & editing. **Zhifeng Jiang:** Formal analysis, Funding acquisition, Methodology, Resources, Writing - review & editing. **Xiaolei Qu:** Formal analysis, Funding acquisition, Methodology, Resources, Supervision, Writing - review & editing. **Po Keung Wong:** Formal analysis, Methodology, Resources, Supervision, Writing - review & editing.

Declaration of Competing Interest

The authors declare that they have no known competing financial interests or personal relationships that could have appeared to influence the work reported in this paper.

Data Availability

Data will be made available on request.

Acknowledgements

This work was supported by the National Key Research and Development Program of China (2020YFC1807002 and 2019YFC1804201), the National Natural Science Foundation of China (Grant 22002059, 21876075, 22178149 and 21622703), Jiangsu Province Natural Science Foundation for Outstanding Youth Scientists (BK20211599), Jiangsu Distinguished Professor Program, and Scientific Research Startup Foundation of Jiangsu University (Grant No. 202096).

Appendix A. Supporting information

Supplementary data associated with this article can be found in the online version at doi:10.1016/j.apcatb.2022.122031.

References

- [1] J. Li, W.F. Pan, Q.Y. Liu, Z.Q. Chen, Z.J. Chen, X.Z. Feng, H. Chen, Interfacial engineering of Bi₁₉Br₃S₂₇ nanowires promotes metallic photocatalytic CO₂ reduction activity under near-Infrared light irradiation, *J. Am. Chem. Soc.* 143 (2021) 6551–6559, <https://doi.org/10.1021/jacs.1c01109>.
- [2] Z. Tang, F.F. Zhu, J.C. Zhou, W.S. Chen, K. Wang, M.C. Liu, N. Wang, N.X. Li, Monolithic NF@ZnO/Au@ZIF-8 photocatalyst with strong photo-thermal-magnetic coupling and selective-breathing effects for boosted conversion of CO₂ to CH₄, *Appl. Catal. B Environ.* 309 (2022), 121267, <https://doi.org/10.1016/j.apcatb.2022.121267>.
- [3] X. Wu, Y. Li, G. Zhang, H. Chen, J. Li, K. Wang, Y. Pan, Y. Zhao, Y. Sun, Y. Xie, Photocatalytic CO₂ conversion of Mo_{0.33}WO₃ directly from the air with high selectivity: Insight into full spectrum-induced reaction mechanism, *J. Am. Chem. Soc.* 141 (2019) 5267–5274, <https://doi.org/10.1021/jacs.8b12928>.
- [4] Z.R. Miao, Q.L. Wang, Y.F. Zhang, L.P. Meng, X.X. Wang, In situ construction of S-scheme AgBr/BiOBr heterojunction with surface oxygen vacancy for boosting photocatalytic CO₂ reduction with H₂O, *Appl. Catal. B Environ.* 301 (2022), 120802, <https://doi.org/10.1016/j.apcatb.2021.120802>.
- [5] X.L. Zhang, C.W. Liu, Y. Zhao, L.B. Li, Y. Chen, F. Raziq, L. Qiao, S.X. Guo, C. Y. Wang, G.G. Wallace, A.M. Bond, J. Zhang, Atomic nickel cluster decorated defect-rich copper for enhanced C₂ product selectivity in electrocatalytic CO₂ reduction, *Appl. Catal. B Environ.* 291 (2021), 120030, <https://doi.org/10.1016/j.apcatb.2021.120030>.
- [6] B.H. Lee, E. Gong, M. Kim, S. Park, H.R. Kim, J. Lee, E. Jung, C.W. Lee, J. Bok, Y. Jung, Y.S. Kim, K.S. Lee, S.P. Cho, J.W. Jung, C.H. Cho, S. Lebeque, K.T. Nam, H. Kim, S.I. In, T. Hyeon, Electronic interaction between transition metal single-atoms and anatase TiO₂ boosts CO₂ photoreduction with H₂O, *Energy Environ. Sci.* 15 (2022) 601–609, <https://doi.org/10.1039/D1EE01574E>.
- [7] Y.X. Li, M.M. Wen, Y. Wang, G. Tian, C.Y. Wang, J.C. Zhao, Plasmonic hot electrons from oxygen vacancies for infrared light-driven catalytic CO₂ reduction on Bi₂O_{3-x}, *Angew. Chem. Int. Ed.* 60 (2021) 910–916, <https://doi.org/10.1002/anie.202010156>.
- [8] Y.J. Zhang, Z.F. Xu, Q. Wang, W.C. Hao, X.P. Zhai, X. Fei, X.J. Huang, Y.P. Bi, Unveiling the activity origin of ultrathin BiOCl nanosheets for photocatalytic CO₂ reduction, *Appl. Catal. B Environ.* 299 (2021), 120679, <https://doi.org/10.1016/j.apcatb.2021.120679>.
- [9] S.C. Chen, H. Wang, Z. Kang, S. Jin, X.D. Zhang, X. Zheng, Z. Qi, J. Zhu, B.C. Pan, Y. Xie, Oxygen vacancy associated single-electron transfer for photofixation of CO₂ to long-chain chemicals, *Nat. Commun.* 10 (2019) 788–795, <https://doi.org/10.1038/s41467-019-08697-x>.
- [10] E. Gong, S. Ali, C.B. Hiragond, H.S. Kim, N.S. Powar, D. Kim, H. Kim, S.I. In, Solar fuels: research and development strategies to accelerate photocatalytic CO₂ conversion into hydrocarbon fuels, *Energy Environ. Sci.* 15 (2022) 880–937, <https://doi.org/10.1039/D1EE02714J>.
- [11] Z.L. Tang, W.J. He, Y.L. Wang, Y.C. Wei, X.L. Yu, J. Xiong, X. Wang, X. Zhang, Z. Zhao, J. Liu, Ternary heterojunction in RGO-coated Ag/Cu₂O catalysts for boosting selective photocatalytic CO₂ reduction into CH₄, *Appl. Catal. B Environ.* 311 (2022), 121371, <https://doi.org/10.1016/j.apcatb.2022.121371>.
- [12] J. Xiong, J. Di, H.M. Li, Interface engineering in low-dimensional bismuth-based materials for photoreduction reactions, *J. Mater. Chem. A* 9 (2021) 2662–2677, <https://doi.org/10.1039/D0TA10549J>.
- [13] J. Xiong, P. Song, J. Di, H.M. Li, Ultrathin structured photocatalysts: a versatile platform for CO₂ reduction, *Appl. Catal. B Environ.* 256 (2019), 117788, <https://doi.org/10.1016/j.apcatb.2019.117788>.
- [14] S.M. Sun, M. Watanabe, J. Wu, Q. An, T. Ishihara, Ultrathin WO₃·0.33H₂O nanotubes for CO₂ photoreduction to acetate with high selectivity, *J. Am. Chem. Soc.* 140 (2018) 6474–6482, <https://doi.org/10.1021/jacs.8b03316>.
- [15] H.J. Yu, J.Y. Li, Y.H. Zhang, S.Q. Yang, K.L. Han, F. Dong, T.Y. Ma, H.W. Huang, Three-in-one oxygen vacancies: Whole visible-spectrum absorption, efficient charge separation, and surface site activation for robust CO₂ photoreduction, *Angew. Chem. Int. Ed.* 58 (2019) 3880–3884, <https://doi.org/10.1002/anie.201813967>.
- [16] Y.F. Li, F. Cui, M.B. Ross, D. Kim, Y.C. Sun, P.D. Yang, Structure-sensitive CO₂ electroreduction to hydrocarbons on ultrathin 5-fold twinned copper nanowires, *Nano Lett.* 17 (2017) 1312–1317, <https://doi.org/10.1021/acs.nanolett.6b05287>.
- [17] Q.Y. Bi, K.Y. Hu, J.C. Chen, Y.R. Zhang, M.S. Riaz, J. Xu, Y.F. Han, F.Q. Huang, Black phosphorus coupled black titania nanocomposites with enhanced sunlight absorption properties for efficient photocatalytic CO₂ reduction, *Appl. Catal. B Environ.* 295 (2021), 120211, <https://doi.org/10.1016/j.apcatb.2021.120211>.
- [18] S.Y. Wang, X. Hai, X. Ding, K. Chang, Y.G. Xiang, X.G. Meng, Z.X. Yang, H. Chen, J. H. Ye, Light-switchable oxygen vacancies in ultrafine Bi₅O₇Br nanotubes for boosting solar-driven nitrogen fixation in pure water, *Adv. Mater.* 29 (2017) 1701774, <https://doi.org/10.1002/adma.201701774>.
- [19] P.S. Li, Z.A. Zhou, Q. Wang, M. Guo, S.W. Chen, J.X. Low, R. Long, W. Liu, P. R. Ding, Y.Y. Wu, Y.J. Xiong, Visible-light-driven nitrogen fixation catalyzed by Bi₅O₇Br nanostructures: Enhanced performance by oxygen vacancies, *J. Am. Chem. Soc.* 142 (2020) 12430–12439, <https://doi.org/10.1021/jacs.0c05097>.

- [20] J. Xiong, P. Song, J. Di, H.M. Li, Bismuth-rich bismuth oxyhalides: a new opportunity to trigger high-efficiency photocatalysis, *J. Mater. Chem. A* 8 (2020) 21434–21454, <https://doi.org/10.1039/D0TA06044E>.
- [21] H. Li, J. Shang, Z.H. Ai, L.Z. Zhang, Efficient visible light nitrogen fixation with BiOBr nanosheets of oxygen vacancies on the exposed {001} facets, *J. Am. Chem. Soc.* 137 (2015) 6393–6399, <https://doi.org/10.1021/jacs.5b03105>.
- [22] Z.Z. Zhang, Y.H. Zhao, J.T. Shen, Z.W. Pan, Y.F. Guo, P.K. Wong, H.B. Yu, Synthesis of 1D Bi₁₂O₁₇Cl_xBr_{2-x} nanotube solid solutions with rich oxygen vacancies for highly efficient removal of organic pollutants under visible light, *Appl. Catal. B Environ.* 269 (2020), 118774, <https://doi.org/10.1016/j.apcatb.2020.118774>.
- [23] T.Y. Kim, W.J. Kim, S.H. Hong, J.E. Kim, K.S. Suh, Ionic-liquid-assisted formation of silver nanowires, *Angew. Chem. Int. Ed.* 48 (2009) 3806–3809, <https://doi.org/10.1002/anie.200806379>.
- [24] J. Zhang, R. Yin, Q. Shao, T. Zhu, X. Huang, Oxygen vacancies in amorphous InO_x nanoribbons enhance CO₂ adsorption and activation for CO₂ electroreduction, *Angew. Chem. Int. Ed.* 58 (2019) 5609–5613, <https://doi.org/10.1002/anie.201900167>.
- [25] H. Han, S. Jin, S. Park, Y. Kim, D. Jang, M.H. Seo, W.B. Kim, Plasma-induced oxygen vacancies in amorphous MnO_x boost catalytic performance for electrochemical CO₂ reduction, *Nano Energy* 79 (2021), 105492, <https://doi.org/10.1016/j.nanoen.2020.105492>.
- [26] P. Kong, H. Tan, T.Y. Lei, J. Wang, W.J. Yan, R.Y. Wang, E.R. Wacławik, Z. F. Zheng, Z. Li, Oxygen vacancies confined in conjugated polyimide for promoted visible-light photocatalytic oxidative coupling of amines, *Appl. Catal. B Environ.* 272 (2020), 118964, <https://doi.org/10.1016/j.apcatb.2020.118964>.
- [27] H. Wang, D.Y. Yong, S.C. Chen, S.L. Jiang, X.D. Zhang, W. Shao, Q. Zhang, W. S. Yan, B.C. Pan, Y. Xie, Oxygen-vacancy-mediated exciton dissociation in BiOBr for boosting charge-carrier-involved molecular oxygen activation, *J. Am. Chem. Soc.* 137 (2018) 1760–1766, <https://doi.org/10.1021/jacs.7b10997>.
- [28] C. Li, H. Jang, M.G. Kim, L.Q. Hou, X.E. Liu, J. Cho, Ru-incorporated oxygen-vacancy-enriched MoO₂ electrocatalysts for hydrogen evolution reaction, *Appl. Catal. B Environ.* 307 (2022), 121204, <https://doi.org/10.1016/j.apcatb.2022.121204>.
- [29] S.L. Wang, S.H. Lin, D.Q. Zhang, G.S. Li, M.K.H. Leung, Controlling charge transfer in quantum-size titania for photocatalytic applications, *Appl. Catal. B Environ.* 215 (2017) 85–92, <https://doi.org/10.1016/j.apcatb.2017.05.043>.
- [30] W.C. Huo, X.A. Dong, J.Y. Li, M. Liu, X.Y. Liu, Y.X. Zhang, F. Dong, Synthesis of Bi₂WO₆ with gradient oxygen vacancies for highly photocatalytic NO oxidation and mechanism study, *Chem. Eng. J.* 361 (2019) 129–138, <https://doi.org/10.1016/j.cej.2018.12.071>.
- [31] Z.G. Geng, X.D. Kong, W.W. Chen, H.Y. Su, Y. Liu, F. Cai, G.X. Wang, J. Zeng, Oxygen Vacancies in ZnO Nanosheets Enhance CO₂ Electrochemical Reduction to CO, *Angew. Chem. Int. Ed.* 57 (2018) 6054–6059, <https://doi.org/10.1002/anie.201711255>.
- [32] S. Guo, J. Di, C. Chen, C. Zhu, M.L. Duan, C. Lian, M.X. Ji, W. Zhou, M.Z. Xu, P. Song, R. Long, X. Cao, K.Z. Gu, J.X. Xia, H.L. Liu, Y. Zhao, L. Song, Y.J. Xiong, S. Z. Li, Z. Liu, Oxygen vacancy mediated bismuth stannate ultra-small nanoparticle towards photocatalytic CO₂-to-CO conversion, *Appl. Catal. B Environ.* 276 (2020), 119156, <https://doi.org/10.1016/j.apcatb.2020.119156>.
- [33] F. Chen, Z.Y. Ma, L.Q. Ye, T.Y. Ma, T.R. Zhang, Y.H. Zhang, H.W. Huang, Macroscopic spontaneous polarization and surface oxygen vacancies collaboratively boosting CO₂ photoreduction on BiOIO₃ single crystals, *Adv. Mater.* 32 (2020) 1908350, <https://doi.org/10.1002/adma.201908350>.
- [34] J. Wu, X.D. Li, W. Shi, P.Q. Ling, Y.F. Sun, X.C. Jiao, S. Gao, L. Liang, J.Q. Xu, W. S. Yan, C.M. Wang, Y. Xie, Efficient visible-light-driven CO₂ reduction mediated by defect-engineered BiOBr atomic layers, *Angew. Chem. Int. Ed.* 57 (2018) 8719–8723, <https://doi.org/10.1002/anie.201803514>.
- [35] G.B. Liu, Z.H. Li, J.J. Shi, K. Sun, Y.J. Ji, Z.G. Wang, Y.F. Qiu, Y.Y. Liu, Z.J. Wang, P.A. Hu, Black reduced porous SnO₂ nanosheets for CO₂ electroreduction with high formate selectivity and low overpotential, *Appl. Catal. B Environ.* 260 (2020), 118134, <https://doi.org/10.1016/j.apcatb.2019.118134>.
- [36] L. Hao, L. Kang, H.W. Huang, L.Q. Ye, K.L. Han, S.Q. Yang, H.J. Yu, M. Batmunkh, Y.H. Zhang, T.Y. Ma, Surface-halogenation-induced atomic-site activation and local charge separation for superb CO₂ photoreduction, *Adv. Mater.* 31 (2019) 1900546, <https://doi.org/10.1002/adma.201900546>.
- [37] X. Li, J.G. Yu, M. Jaroniec, X.B. Chen, Cocatalysts for selective photoreduction of CO₂ into solar fuels, *Chem. Rev.* 119 (2019) 3962–4179, <https://doi.org/10.1021/acs.chemrev.8b00400>.
- [38] H.J. Yu, F. Chen, X.W. Li, H.W. Huang, Q.Y. Zhang, S.Q. Su, K.Y. Wang, E.Y. Mao, B. Mei, G.D. Mu, T.Y. Ma, Y.H. Zhang, Synergy of ferroelectric polarization and oxygen vacancy to promote CO₂ photoreduction, *Nat. Commun.* 12 (2021) 4594, <https://doi.org/10.1038/s41467-021-24882-3>.
- [39] X.J. Ren, M.C. Gao, Y.F. Zhang, Z.Z. Zhang, X.Z. Cao, B.Y. Wang, X.X. Wang, Photocatalytic reduction of CO₂ on BiOX: Effect of halogen element type and surface oxygen vacancy mediated mechanism, *Appl. Catal. B Environ.* 274 (2020), 119063, <https://doi.org/10.1016/j.apcatb.2020.119063>.
- [40] X. Shi, X.A. Dong, Y. He, P. Yan, S.H. Zhang, F. Dong, Photoswitchable chlorine vacancies in ultrathin Bi₄O₅Cl₂ for selective CO₂ photoreduction, *ACS Catal.* 12 (2022) 3965–3973, <https://doi.org/10.1021/acscatal.2c00157>.
- [41] X.L. Zu, Y. Zhao, X.D. Li, R.H. Chen, W.W. Shao, Z.Q. Wang, J. Hu, J.F. Zhu, Y. Pan, Y.F. Sun, Y. Xie, Ultrastable and efficient visible-light-driven CO₂ reduction triggered by regenerative oxygen-vacancies in Bi₂O₂CO₃ nanosheets, *Angew. Chem. Int. Ed.* 60 (2021) 13840–13846, <https://doi.org/10.1002/ange.202101894>.
- [42] J.L. Zhao, Z.R. Miao, Y.F. Zhang, G.Y. Wen, L.H. Liu, X.X. Wang, X.Z. Cao, B. Y. Wang, Oxygen vacancy-rich hierarchical BiOBr hollow microspheres with dramatic CO₂ photoreduction activity, *J. Colloid Interface Sci.* 593 (2021) 231–243, <https://doi.org/10.1016/j.jcis.2021.02.117>.
- [43] J. Wang, T. Bo, B. Shao, Y. Zhang, L. Jia, X. Tan, W. Zhou, T. Yu, Effect of S vacancy in Cu₃SnS₄ on high selectivity and activity of photocatalytic CO₂ reduction, *Appl. Catal. B Environ.* 297 (2021), 120498, <https://doi.org/10.1016/j.apcatb.2021.120498>.
- [44] L. Liang, X.D. Li, J.C. Zhang, P.Q. Ling, Y.F. Sun, C.M. Wang, Q. Zhang, Y. Pan, Q. Xu, J.F. Zhu, Y. Luo, Y. Xie, Efficient infrared light induced CO₂ reduction with nearly 100% CO selectivity enabled by metallic CoN porous atomic layers, *Nano Energy* 69 (2020), 104421, <https://doi.org/10.1016/j.nanoen.2019.104421>.
- [45] H.J. Yu, H.W. Huang, A.H. Reshak, S. Auluck, L.Z. Liu, T.Y. Ma, Y.H. Zhang, Coupling ferroelectric polarization and anisotropic charge migration for enhanced CO₂ photoreduction, *Appl. Catal. B Environ.* 284 (2021), 119709, <https://doi.org/10.1016/j.apcatb.2020.119709>.
- [46] B.Y. Xu, Y. An, Y.Y. Liu, X.Y. Qin, X.Y. Zhang, Y. Dai, Z.Y. Wang, P. Wang, M. H. Whangbo, B.B. Huang, Enhancing the photocatalytic activity of BiOX (X = Cl, Br, and I), (BiO)₂CO₃ and Bi₂O₃ by modifying their surfaces with polar organic anions, 4-substituted thiophenolates, *J. Mater. Chem. A* 5 (2017) 14406–14414, <https://doi.org/10.1039/C7TA03970K>.
- [47] D.J. Mao, S.S. Ding, L.J. Meng, Y.X. Dai, C. Sun, S.G. Yang, H. He, One-pot microemulsion-mediated synthesis of Bi-rich Bi₄O₅Br₂ with controllable morphologies and excellent visible-light photocatalytic removal of pollutants, *Appl. Catal. B Environ.* 207 (2017) 153–165, <https://doi.org/10.1016/j.apcatb.2017.02.010>.
- [48] B. Wang, S.Z. Yang, H.L. Chen, Q. Gao, Y.X. Weng, W.S. Zhu, G.P. Liu, Y. Zhang, Y. Z. Ye, H.Y. Zhu, H.M. Li, J.X. Xia, Revealing the role of oxygen vacancies in bimetallic PbBiO₂Br atomic layers for boosting photocatalytic CO₂ conversion, *Appl. Catal. B Environ.* 277 (2020), 119170, <https://doi.org/10.1016/j.apcatb.2020.119170>.
- [49] Y.B. Shi, G.M. Zhan, H. Li, X.B. Wang, X.F. Liu, L.J. Shi, K. Wei, C.C. Ling, Z.L. Li, H. Wang, C.L. Mao, X. Liu, L.Z. Zhang, Simultaneous manipulation of bulk excitons and surface defects for ultrastable and highly selective CO₂ photoreduction, *Adv. Mater.* 33 (2021) 2100143, <https://doi.org/10.1002/adma.202100143>.
- [50] D.J. Mao, J.L. Yuan, X.L. Qu, C. Sun, S.G. Yang, H. He, Size tunable Bi₃O₄Br hierarchical hollow spheres assembled with {001}-facets exposed nanosheets for robust photocatalysis against phenolic pollutants, *J. Catal.* 369 (2019) 209–221, <https://doi.org/10.1016/j.jcat.2018.11.016>.
- [51] S.B. Wang, B.Y. Guan, X.W. Lou, Construction of ZnIn₂S₄-In₂O₃ Hierarchical tubular heterostructures for efficient CO₂ photoreduction, *J. Am. Chem. Soc.* 140 (2018) 5037–5040, <https://doi.org/10.1021/jacs.8b02200>.